Available online at www.sciencedirect.com
ScienceDirect
Journal of Solid State Chemistry 180 (2007) 2905–2915
JOURNAL OF SOLID STATE CHEMISTRY
www.elsevier.com/locate/jssc

The influence of cobalt doping on photocatalytic nano-titania: Crystal chemistry and amorphicity

Suo Hon Lim[a,*], Cristiano Ferraris[a,b], Martin Schreyer[a], Kaimin Shih[c], James O. Leckie[c], T.J. White[a]

[a]*The School of Materials Science and Engineering, Nanyang Technological University, Block N4.1, 50 Nanyang Avenue, 639798, Singapore, Singapore*
[b]*Laboratoire de Minéralogie, USM 201, Muséum National d'Histoire Naturelle, CP 52, 61 Rue Buffon, 75005 Paris, France*
[c]*The Department of Civil and Engineering, Stanford University, Terman Engineering Center, Stanford, CA 94305-4020, USA*

Received 27 March 2007; received in revised form 27 July 2007; accepted 10 August 2007
Available online 4 September 2007

Abstract

Photocatalysts of nominal composition $(Ti_{1-x}Co_x)O_{2-\delta}$ with $0.001 \leqslant x \leqslant 0.05$ were prepared via a sol–gel technique followed by air firing (200–1000 °C). The incorporation of cobalt inhibited crystal growth and slightly raised the anatase to rutile transformation temperature (~700 °C). An amorphous component was invariably significant with the maximum content (41–53 wt%) appearing simultaneously with the removal of anatase, suggesting that rutile crystallizes via an aperiodic structure. While the introduction of cobalt shifted the apparent band gap to visible light energies this did not enhance performance as there was limited miscibility of cobalt in titania, non-catalytic secondary phases were present, and active Ti^{3+} sites were displaced by cobalt.

Keywords: Anatase; Rutile; Amorphous content; Photocatalytic activity; Methylene blue; Formic acid

1. Introduction

Titanium oxides (titania) in various polymorphic and physical forms find application in air and water purification, as pigments, gas sensors and antimicrobial agents, and as corrosion resistant and non-toxic photocatalytic materials [1–4]. However, effective photoexcitation requires irradiation at wavelengths <400 nm, where photon energies are similar to the semiconductor band gaps of the common polymorphs anatase (3.2 eV, $\lambda \leqslant 385$ nm) and rutile (3.02 eV, $\lambda \leqslant 410$ nm) [5–6]. Consequently, while excitation is efficient under ultraviolet (UV) sources, it is rather less so when exploiting the ~5% UV fraction of sunlight. Therefore, it would be advantageous technically and economically to reduce the band gap energy to extend catalytic activation deep into the visible range.

One method to induce bathochromic (red) shifts of the band gap is the well established process of chemically doping titania to introduce either anions (X) such as F^-, N^{3-}, C^{4-} or S^{2-} to produce oxygen deficient titanias ($TiO_{2-\delta}X_{2\delta/n}$), or cations (A) including $Co^{2+,3+}$, Ag^+, Pt^{6+}, W^{6+} and V^{5+} to form $Ti_{1-x}A_xO_{2-\delta}$ compounds [5–12]. In all these cases, superior catalytic activity is generally taken to indicate that crystallochemical modification of titania has been achieved though aliovalent or altervalent substitutions such as $O^{2-} \leftrightarrow S^{2-}$, $Ti^{4+} \leftrightarrow Co^{4+}$, $Ti^{4+}O^{2-} \leftrightarrow Co^{3+}F^-$, or $Ti^{4+}O^{2-} \leftrightarrow W^{6+}C^{4-}$. However, direct evidence of such replacements is not usually presented, as small crystallite sizes, low dopant concentrations, and the difficulties of conducting microanalysis (especially of anions) makes verification particularly challenging. A further issue, that to date has not received significant attention is the role of amorphous phases, which may co-exist with rutile and anatase, especially when soft chemical routes are used for synthesis.

It has been reported that cobalt doping of titania will enhance photocatalytic properties. Barakat et al. [11] found that titania containing 0.036 mol% cobalt rapidly photo-oxidised 2-chlorophenol, with greater or lesser amounts

*Corresponding author. Fax: +65 67909081.
E-mail address: shlim@ntu.edu.sg (S.H. Lim).

0022-4596/$ - see front matter © 2007 Elsevier Inc. All rights reserved.
doi:10.1016/j.jssc.2007.08.021

proving less active. While it was not possible to conclude if cobalt was entering titania substitutionally, or present as a discrete oxide, it was shown that after high temperature firing rutile (TiO_2) and ilmenite-type $Co^{2+}Ti^{4+}O_3$ co-existed. Broadly similar results were obtained by Iwasaki et al. [12] who studied the degradation of acetaldehyde. Although cobalt-doped titania is frequently reported as $[Ti_{1-x}Co_x]O_2$, this formulation is evidently only correct for tetravalent cobalt (a rare valence state), whereas both experiment [11] and theory [13] suggest di- or tri-valency are prevalent and a more correct crystallochemical description is $[Ti_{1-x}Co_x]O_{2-\delta}$ [14]. Additionally, these idealized formulas neglect the possibility of metal vacancies that have been recently reported [15] and thoroughly investigated for sol–gel derived titania [16].

In a previous study of titania prepared by hydrolysis of titanium butoxide we confirmed the correlation of crystallographic data derived from Rietveld analysis of powder X-ray diffraction (XRD) patterns with that from high-resolution transmission electron microscopy (TEM), and demonstrated a blue shift in band gap with increasing quantum confinement in nanosized crystals [17]. In this paper, these techniques are used to characterize titanias as a function of cobalt loading and sintering temperature. In addition, the chemical, crystallographic and physical states of cobalt are investigated, with particular attention given to the abundance and role of X-ray amorphous materials. General protocols for the use of methylene blue and formic acid as target compounds for studying photocatalytic activity in UV and visible light are given, and the performance of cobaltiferous titania benchmarked against pure titania prepared under identical conditions. In this way, comparisons can be drawn between compounds that are strongly adsorbed and perhaps partially reacted (methylene blue) and those that degrade directly without the formation of intermediates (formic acid). The manner in which cobalt loading influences the anatase to rutile transformation, crystal growth, and specific surface area are also reported.

2. Experimental methods

2.1. Material synthesis

Oxides of nominal composition $(Ti_{1-x}Co_x)O_{2-\delta}$ were synthesized via a sol–gel technique with $x = 0.001$, 0.005, 0.01, 0.02 and 0.05 (Fig. 1). Titanium tetrabutoxide [Ti(O-Bu)$_4$, 97%, Aldrich] was dissolved in absolute ethanol (EtOH, >99.9%, Merck) prior to hydrolysis, with cobalt introduced by adding a solution of absolute EtOH, anhydrous $CoCl_2$ (Merck), HCl (37%, Merck) and deionized water dropwise. The molar ratio of EtOH, deionized water and HCl was fixed at 15, 1 and 0.3 for all the cobalt-doped titanias. The sol was homogenized by stirring for 30 min at room temperature followed by gelation for 5 days. The gel was vacuum dried at 60 °C then calcined at selected temperatures from 200 to 1000 °C for 2 h. The heat-treated samples were washed with hot water to remove chloride before using as a photocatalyst. The sample codes are collated in Table 1.

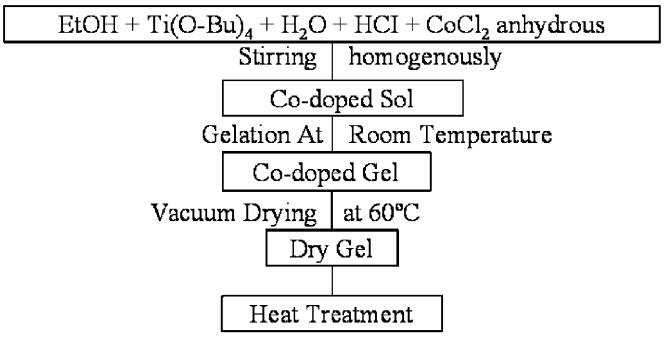

Fig. 1. Flow sheet for photocatalyst synthesis.

Table 1
Metals content of $(Ti_{1-x}Co_x)O_{2-\delta}$ compounds

Sample code	Nominal composition		
	Co(x)	Ti	Co/Ti
Co001	0.001	0.999	0.001
Co005	0.005	0.995	0.005
Co01	0.01	0.99	0.0101
Co02	0.02	0.98	0.0204
Co05	0.05	0.95	0.0526

2.2. Materials characterization

XRD patterns with angular range of 10–140° were collected using Bragg–Brentano geometry (Cu$K\alpha$ source, primary and secondary soller slits, 0.1 mm divergence slits, 0.3 mm receiving slit, secondary graphite monochromator) with a Shimadzu Lab-XRD-6000 instrument. The diffractometer resolution was refined by measurement of standard LaB_6 (NIST SRM 660a) employing the fundamental parameter approach as implemented in TOPAS [18–19]. Quantitative phase analyses using the Rietveld method included refinement of the background, surface roughness according to Suortti [20], cell constants, scale factors, titanium occupancy (anatase) and crystallite size. All atomic co-ordinates and thermal parameters were kept fixed to the values of the starting models of the crystalline phases that included anatase [21], rutile [22] and $CoTiO_3$ [23]. The mass of amorphous material and the relative values of the cell parameters were determined by adding 30 wt% of Al_2O_3 (NIST SRM 676) as an internal standard. The amorphous content of SRM 676 has recently been corrected from 2% to 8.25% [24] and the calculations adjusted accordingly. Every sample was homogenized with the Al_2O_3 standard by 20 min of manual grinding in an agate mortar to avoid the need to apply a correction for microabsorption. The following refinement strategy was employed: 1/x background function and a Chebychev

polynomial of order 4; lattice constants (a and c) of alumina fixed at 4.75919 and 12.99183 Å provided by NIST [24] and atomic parameters according to Toebbens et al. [25]; zero shift, sample displacement, lattice parameters, scale factors and crystallite size of anatase, rutile and ilmenite optimized in turn. The isothermal parameters of all phases were constrained to literature values. For anatase, the titanium occupancy was refined, as Grey and Wilson [16] had shown substantial metal vacancies in sol–gel derived material. However, this earlier study used the atomic form factor of Ti^{2+}, rather than Ti^{4+} to model the vacancies, as this gave a better match for well-crystallized anatase where full titanium occupation was presumed. In the present refinements, the form factor of Ti^{4+} was used throughout.

Powdered samples deposited onto holey carbon coated copper grids were analyzed using TEM performed at 200 kV on a JEOL JEM 2100F microscope, equipped with double-tilt holder. Field limiting apertures used for selected area electron diffraction (SAED) were 5, 20 and 60 μm in diameter. High-resolution images were collected using a high-contrast objective aperture of 20 μm, corresponding to a nominal point-to-point resolution of 0.17 nm.

The chemical states of surface cobalt and titanium were evaluated by X-ray photoelectron spectroscopy (XPS) using a PHI 5600 instrument and a magnesium anode. Survey scans covered the binding energy from 0 to 1000 keV calibrated against adventitious carbon, and the multiplex spectra processed using computer aided surface analysis (CASA) software [26].

Differential scanning calorimetry—thermogravimetric analysis (DSC-TG) (Netzsch 409) established decomposition and crystallization temperatures, thermal stability, and phase transformations of the dry gels. Samples were heated to 1000 °C at a rate of 5 °C per min^{-1}, with nitrogen used as both the balance and sample gas at a flow rate of 50ml per min^{-1}. Fourier transform infrared spectrometry (FTIR) (Perkin Elmer GX) was used to detect organic residues in the samples calcined from 200 up to 800 °C after being well-ground with potassium bromide (KBr, IR grade, Merck) and pressed into pellets (10 mm diameter). Specific surface area was determined using the Brunauer–Emmett–Teller (BET) physisorption method (Micromeritics ASAP 2020). Prior to collection of the final isotherm data, the powders were degassed overnight at 250 °C, except for those materials calcined at 200 °C, where the degassing temperature was reduced to 150 °C to avoid alteration.

Photocatalytic activity of cobalt-doped titania was investigated by monitoring the photodegradation of methylene blue and formic acid as a function of reaction time under UV and visible light. Two protocols were established for the photooxidation of methylene blue (Protocol 1) and formic acid (Protocol 2) with NaCl (aq) introduced in the former to remove the influence of colloidal scattering during UV–visible spectroscopy measurement. In Protocol 2, data calibration by chloride was carried out after each capillary electrophoresis measurement. The reactor schematics and experimental procedures of these photocatalytic tests are deposited as supplementary information.

3. Results

3.1. Materials properties

3.1.1. Phase transitions

The X-ray amorphous dry gel powders crystallize as anatase when heated to 200 °C and subsequently convert to rutile at higher calcination temperatures such that the onset of the phase transition increases to 700 °C with cobalt doping (Fig. 2) as compared to a previous study of pure titania (600 °C) [17]. In addition, ilmenite-type $Co^{2+}Ti^{4+}O_3$ appears at the highest cobalt concentrations and firing temperatures. On the basis of diffraction peak broadening, anatase crystals obtained at 200 °C have thicknesses of ~5 nm that expand to 20–30 nm at 600 °C with growth suppressed marginally at higher cobalt levels. For calcination at 800 °C, Co01 ($x = 0.01$) contained trace $CoTiO_3$ (1.75 wt%, ~76 nm) with substantially more found

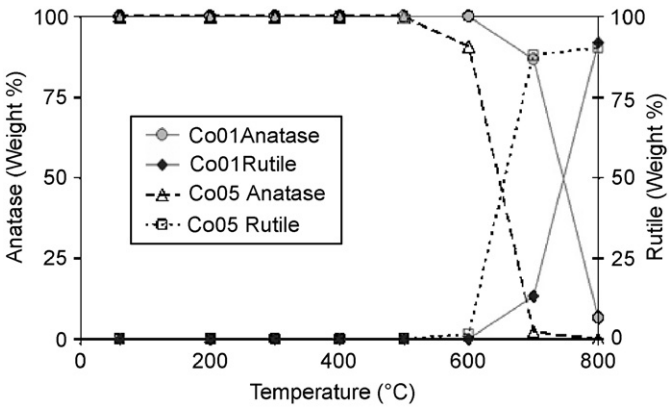

Fig. 2. The evolution of weight% of anatase and rutile in (a) Co001 and (b) Co05 versus calcination temperatures.

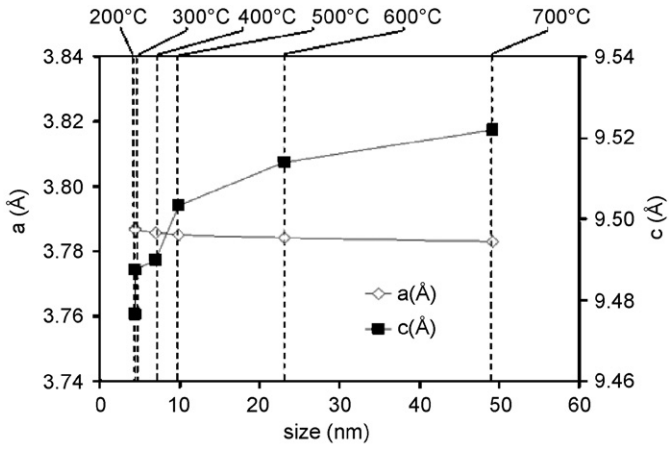

Fig. 3. The evolution of unit cell parameters, a and c, of anatase in Co01 versus crystallite size and annealing temperature.

in Co05 (9.9 wt%, ~97 nm). The '*a*' unit cell parameter of Co-doped titanias decreased from 3.787(4) to 3.783(1) Å, with annealing temperature and crystallite size, while '*c*' increased from 9.478(4) to 9.522(5) Å (Fig. 3). The '*c*' dilation is closely related to crystal growth with the expansion slowing as the crystallite size approaches 100 nm.

Thermal analyses were consistent with the diffraction data showing clear differentiation between high cobalt-doped titanias ($x \geqslant 0.01$) and those containing lower concentrations. The weight loss (40%) and exothermic peaks below 400 °C reflect the oxidative elimination of organic residues and water, while the exothermic reactions between 450 and 550 °C, arise from rapid crystallization of anatase and removal of trace organic compounds. The formation of $CoTiO_3$ for $x = 0.01$, 0.02 and 0.05 corresponds to the exothermic transitions at ~650 and 770 °C. The transformation of anatase to rutile took place in a broad band between 700 and 900 °C.

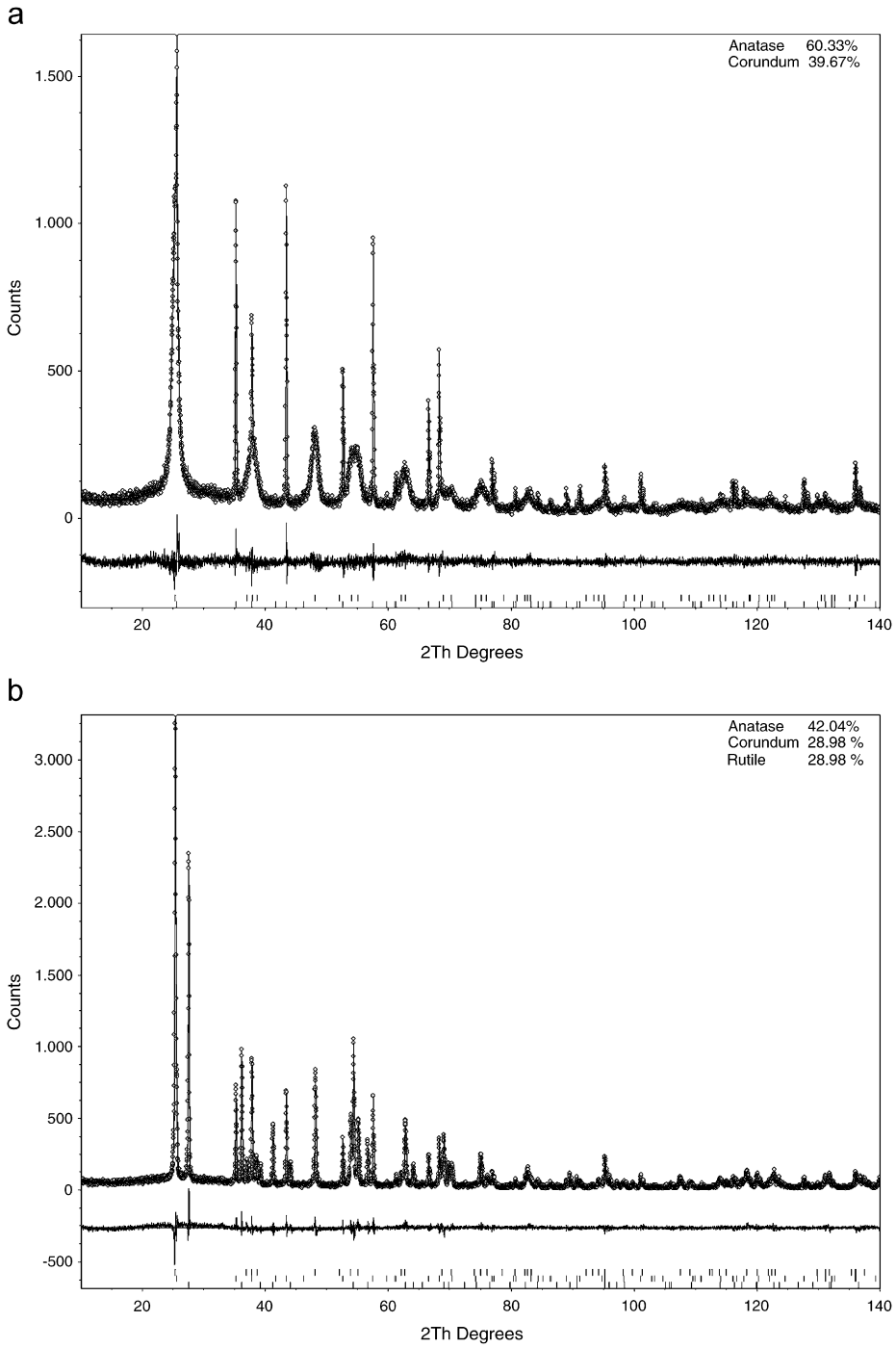

Fig. 4. Quantitative Rietveld refinements of Co01 and 30 wt% of SRM 676 added for the determination of the amorphous content (a) calcined at 400 °C and (b) calcined at 700 °C.

Prior to calcination, FTIR spectroscopy confirmed the presence of physisorbed H_2O with characteristic absorption at 1620 cm^{-1} [17,27,28]. Other features include: (i) free and bounded hydroxyl (O–H) groups of tert-butanol that absorb strongly from 3650 to 3200 cm^{-1}; (ii) out-of-plane bending of the bonded O–H group in the range 769–650 cm^{-1}; (iii) a single band at 1384 cm^{-1} caused by the O–H in-plane bending vibration of the tertiary alcohol [26]; and (iv) C–O stretching absorptions from the band range of 1023–1114 cm^{-1}. After calcination at 200 °C, Co001 showed strong C–H stretching absorption bands of $–CH_3$ at 2853, 2923 and 2951 cm^{-1} and a corresponding disappearance of the O–H group due to the removal of tert-butanol (with a boiling point of 83 °C). Treatment at 400 °C leaves trace organics that disappear at 500 °C in agreement with the DSC-TG observations.

3.1.2. Phase assemblages

In addition to anatase, rutile and ilmenite, significant amorphous content was present at all calcination temperatures. Particularly at high temperatures the existence of non-diffracting content is not intuitively obvious as a characteristic ''amorphous hump'' is absent (Fig. 4b). Quantitative Rietveld analyses showed that samples treated at 200 °C contain 53 wt% amorphous matter, that upon higher temperature treatment initially decreases to 4–25 wt% (Fig. 5). A further increase of calcination temperature leads to a massive augmentation in amorphicity with a maximum of 41–53 wt% at 800 °C when the anatase completely disappears and rutile is the only crystalline phase. In the case of Co001 heating was continued to 1000 °C that reduced the non-diffracting phase to 29 wt%. The phase composition of Co001 and Co01 calcined at different temperatures are summarized in Tables 2a and b. The proportion of Ti-vacancies was refined for anatase. At 200 °C a titanium occupancy of 83(5)% was found which increased to 97(7)% at 300 °C and reached 100% at 500 °C. There was no indication of metal deficiency in rutile. Titanium vacancies have been reported in sol-gel derived anatase by Grey and Wilson [16] where they are stabilized by the presence of hydroxyl anions that are rapidly removed as water vapour on thermal treatment. In this case, cobalt incorporation can be neglected as a secondary effect due to the low concentration of the metal. The sum formula of the deficient anatase can be given as $Ti_{1-x}O_{2-4x}OH_{4x}$ under the assumption that bulk titanium is tetravalent and charge balance is maintained by the substitution of O^{2-} by OH^-, rather than by oxygen defects.

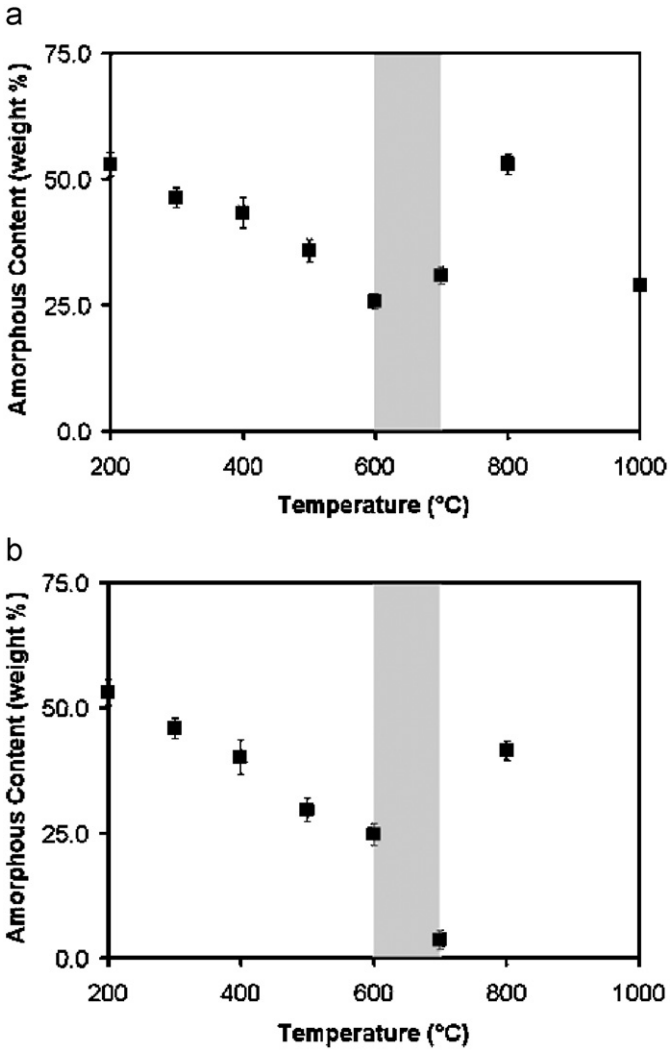

Fig. 5. Temperature dependence of amorphous content: (a) Co001 and (b) Co01.

3.1.3. Microstructure and nanostructure

The material calcined at 200 °C contains nano-crystalline anatase having a mean diameter of ~5 nm (Fig. 6), a

Table 2a
Phase content of Co001 as a function of annealing temperature

Temperature (°C)	Anatase	Rutile	Amorphous
200	47.1	0.0	52.9
300	53.7	0.0	46.3
400	56.6	0.0	43.4
500	64.2	0.0	35.8
600	74.2	0.0	25.8
700	65.6	3.6	30.8
800	0.0	47.1	52.9
1000	0.0	71.1	28.9

Table 2b
Phase content of Co01 as a function of annealing temperature

Temperature (°C)	Anatase	Rutile	Ilmenite	Amorphous
200	46.9	0.0	0.0	53.1
300	54.0	0.0	0.0	46.0
400	59.8	0.0	0.0	40.2
500	70.5	0.0	0.0	29.5
600	75.3	0.0	0.0	24.7
700	57.0	39.3	0.0	3.6
800	0.0	57.3	1.2	41.5

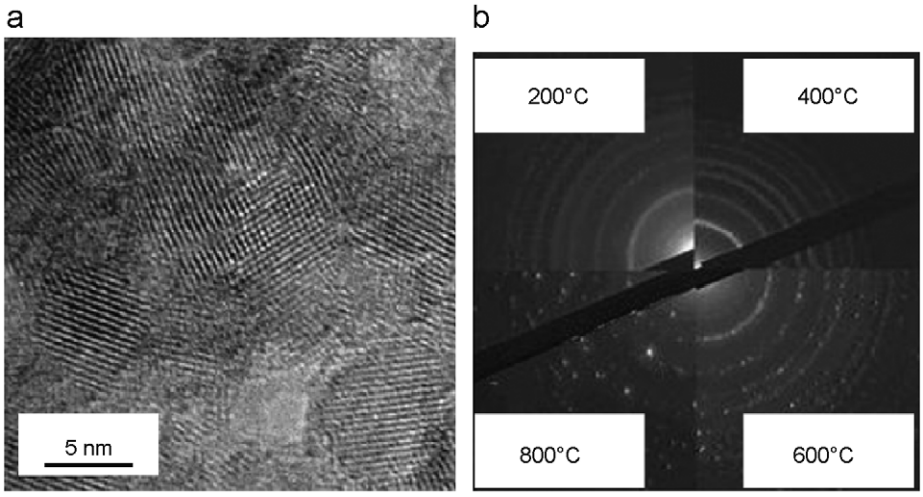

Fig. 6. (a) Lattice image of Co05 calcined at 400 °C and (b) SAED patterns of powders calcined from 200 to 800 °C.

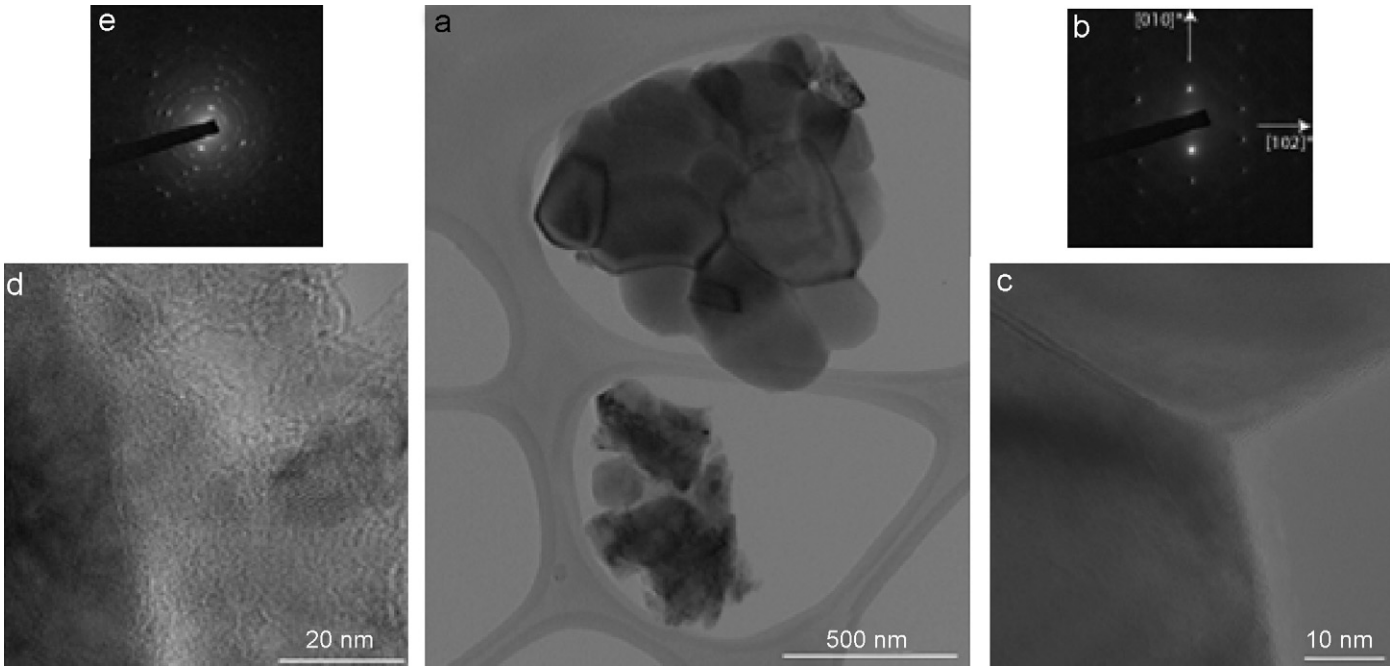

Fig. 7. (a) Bright field images of Co01 calcined at 800 °C; SAED and HRTEM images of sub-micrometric idiomorphic rutile crystals assemblages (b and c) and nano-crystals of rutile embedded amorphous material (d and e).

statistically smaller value compared to the 6–10 nm reported previously for nano-titania without cobalt doping [17]. The crystals grew to 10–12 nm at 400 °C, and further increased from 25 nm at 600 °C to 95 nm at 800 °C. SAED patterns contained featureless rings attributed to anatase at 400 °C, which became progressively differentiated at higher temperatures due to enhanced crystal growth. Of particular interest are results for the sample Co01 calcined at 800 °C for 2 h (Fig. 7). The analyses indicate co-existing (i) sub-micron idiomorphic rutile crystal assemblages (Fig. 7a–c), and (ii) smaller non-idiomorphic rutile crystals (20–25 nm) encapsulated in amorphous material as confirmed by the SAED (Fig. 7d and e). HRTEM shows well-defined crystal

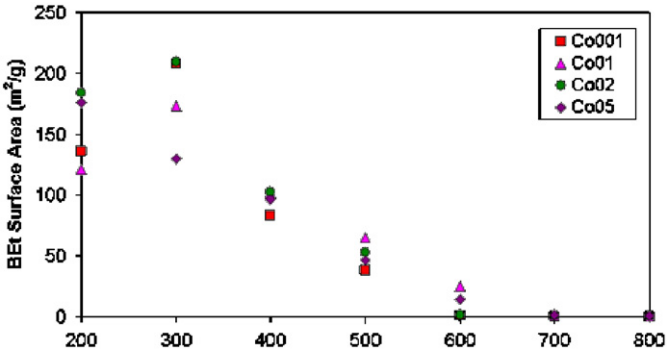

Fig. 8. BET surface area of Co001, Co01, Co02 and Co05. (Error bars are smaller than the symbol size).

Table 3
Chemical states of surface titanium and cobalt

Material		Ti $2p^{3/2}$			Co $2p^{3/2}$	
Cobalt content, x	Firing temperature (°C)	Chemical state	Binding energy (eV)	Atomic (%)	Chemical state	Binding energy (eV)
0	400	Ti^{3+}	456.8	32.9		
		Ti^{4+}	458.7	67.1		
0.001	400	Ti^{3+}	456.8	27.2	Less than lower limit of detection	
		Ti^{4+}	458.7	72.8		
	500	Ti^{3+}	456.8	18.3		
		Ti^{4+}	458.0	81.7		
	800	Ti^{3+}	456.8	14.0		
		Ti^{4+}	457.7	86.0		
0.01	800	Ti^{3+}	456.8	14.0	Mixed Co^{2+} and Co^{3+}	780.1
		Ti^{4+}	458.7	86.0		
0.02	800	Ti^{3+}	456.8	14.3	Mixed Co^{2+} and Co^{3+}	780.9
		Ti^{4+}	458.8	85.7		
0.05	800	Ti^{3+}	456.8	14.1	Mixed Co^{2+} and Co^{3+}	781.5
		Ti^{4+}	458.7	85.9		

habit and irregular surfaces where smaller rutile nanocrystals aggregate (Fig. 7c and d).

The BET surface areas of the Co-doped titanias are summarized in Fig. 8. As noted previously, calcination at 200 °C initiates crystallization of anatase while most organic compounds are oxidized completely after 400 °C. Both processes cause shrinkage, and the loss of CO_2 and H_2O vapour create a sponge-like structure of specific surface areas ranging from 200 m^2/g (200 °C) to 80 m^2/g (400 °C). The isotherm was characterized as Type IV [29] indicating that these materials are mesoporous. A rapid decrease of specific surface area from 300 °C onwards is a consequence of crystallization and growth of anatase. At calcination temperatures >700 °C, the specific surface areas were $<1\,m^2\,g^{-1}$ [30].

3.1.4. Cobalt incorporation

XPS showed that surface titanium in pure and cobalt-doped titania existed primarily as Ti^{4+} with less Ti^{3+} that decreased with cobalt loading and sintering temperature (>500 °C) (Table 3). Cobalt could not be detected at low concentrations ($0.001 \leqslant x \leqslant 0.01$) but for Co01 calcined at 800 °C a Co $2p^{3/2}$ peak at 780.1 eV was evident (Fig. 9, Table 3). The strong paramagnetic satellite peaks are consistent with CoO, Co_2O_3 or mixed-valent Co_3O_4 [31], but the chemical states of cobalt were not been confirmed unambiguously as the binding energies of Co^{2+} and Co^{3+} could not be differentiated. At higher cobalt doping the Co $2p^{3/2}$ spectral lines of Co02 and Co05 were shifted to 780.9 and 781.5 eV. The intensity of Co $2p^{3/2}$ peak increased with the concentration of cobalt. Under the synthesis conditions used, the miscibility of cobalt in titania is limited with $CoTiO_3$ the preferred form, especially at higher temperatures (>700 °C).

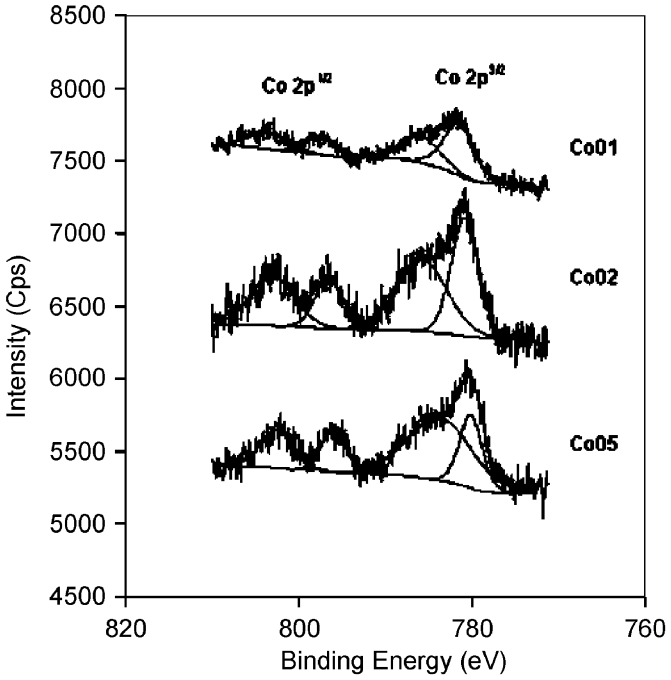

Fig. 9. Co XPS multiplex scan of Co01, Co02 and Co05 calcined at 800 °C.

3.1.5. Band gap

The absorbances of pure titania and Co-doped titania powders in the UV and visible regions (Fig. 10) suggested the band gap energy of the former calcined at 400 °C is 2.97 eV which is lower than the reported value for anatase (3.2 eV) when quantum confinement is operative [6,11]. After cobalt doping the band gaps narrow, although at the highest loadings ($x = 0.05$) it could not be satisfactorily estimated by extrapolation of the spectrum. It is noted that

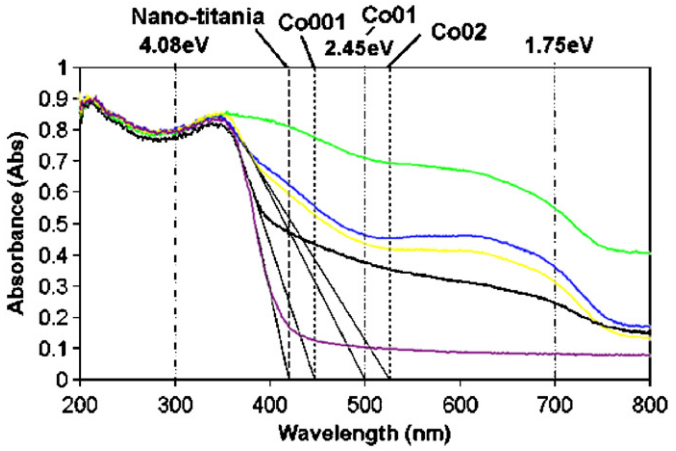

Fig. 10. UV–visible spectra of pure titania and Co-doped titania powders calcined at 400 °C (band gap energy: nano-titania—2.97 eV, Co001—2.74 eV, Co01—2.45 eV and Co02—2.36 eV).

Table 4
Degradation rate constant of nano-titania and Co-doped titania

Composition (x)	Heat treatment	Degradation rate constant (min^{-1})			
		Methylene blue		Formic acid	
		Ultraviolet	Visible	Ultraviolet	Visible
Blank		0.005	Negligible	0.004	Negligible
0	400 °C/2 h	0.067	0.002	0.186	0.001
	400 °C/10 h	0.077	0.001	0.169	0.000
	500 °C/2 h	0.035	0.001	0.092	0.001
0.001	400 °C/2 h	0.075	0.001	0.150	0.001
	400 °C/10 h	0.070	0.001	0.151	Negligible
	500 °C/2 h	0.038	0.001	0.101	0.000
	600 °C/2 h	0.037	0.001	–	–
	700 °C/2 h	0.032	Negligible	–	–
0.01	400 °C/2 h	0.046	0.001	0.088	0.001
0.05	400 °C/2 h	0.025	0.000	0.055	0.001

the Co05 powder was green. However, because at least two phases—crystalline and amorphous—are invariably present the estimation of the band gap energy is of limited value, as the data contains a convolution of absorbances.

3.2. Photocatalytic oxidation

3.2.1. Methylene blue

A blank test using UV light partially bleached ($C/C_o = 0.7$) methylene blue over 60 min^{-1}, but in the presence of pure titania and Co001 catalysts calcined at 400 °C, the suspension was rendered achromatic. For $x > 0.001$ photocatalytic efficiency decreased with the concentration of cobalt, but for all compositions a linear decay of $\ln(C/C_o)$ with irradiation time was consistent with pseudo first order kinetics.

Experiments in visible light yielded rate constants 10^{-3}–10^{-4} slower than in UV light. In relative terms, doping failed to produce enhancement in visible light activity. Pure titania calcined at 400 °C performed best during photo-mineralization of methylene blue under visible light irradiation, with the rate constant of Co001 (which performed well in UV light) being much lower. However, when calcined at 500 °C superior visible light catalysis was observed, possibly because of better crystallization of anatase with surfaces enriched with Ti^{3+} (Table 4).

3.2.2. Formic acid

A blank test demonstrated ~20% photolysis after 60 min^{-1} UV irradiation and a pseudo first order rate constant of 0.004 min^{-1} (Table 4), with pure nano-titania calcined at 400 °C being more effective (0.186 min^{-1}). Co001 calcined at 400 °C degraded formic acid most effectively among the Co-doped materials delivering a rate constant of 0.150 min^{-1}, however, catalytic activity deteriorated at higher cobalt levels, with the $x = 0.05$ material calcined at 400 °C least effective. Unlike the PCO of methylene blue, the degradation rate of formic acid was not influenced by longer calcination times to 10 h at 400 °C. The rate constants of nano-titania and Co001 calcined for 2 and 10 h were similar, but calcination at 500 °C reduced the rate constant to 0.101 min^{-1}.

Under visible light there was negligible degradation of formic acid, and nano-titania calcined at 400 °C had the highest rate constant of 0.001 min^{-1}. There was little improvement in the PCO of formic acid using Co-doped materials calcined at 400 and 500 °C (both at 0.001 min^{-1}) (Table 4). For nano-titania and Co001 calcined at 400 °C with a 10 h holding time, the degradation rate was negligible.

4. Discussion

4.1. Crystal chemistry

Significant amorphous content is possibly ubiquitous in titania synthesized through soft chemical routes. The validity of the quantitative XRD was confirmed by using well crystalline CaF_2 as an alternate spike that delivered a similar amorphous content as the NIST alumina standard for Co001 calcined at 800 °C. Several aspects proved essential for obtaining a reliable quantitative Rietveld analysis: first, the sample and internal standard must be thoroughly homogenized by fine-grinding to avoid micro-absorption effects. Second, scanning over a wide 2θ-range is essential to decouple surface roughness and isothermal parameters. Third, it is advisable to constrain the isothermal parameters of all phases to values obtained from single crystal or neutron data, at least during the early stages of the refinement. Neglecting any of these issues may easily lead to poor estimation of the amorphous content by up to a factor of 2. The standard P25 titania (Degussa) contains 10 wt% of a non-diffracting phase if determined in

exactly the same way as described in this study. For the present sol–gel synthesized titanium dioxides, the findings are best explained by the development of two amorphous phases, rather than one. The first appears as a precursor to anatase during low temperature treatment (200–600 °C), and decreases substantially with the onset of crystallization. Substantial amounts of a second amorphous phase appear as an intermediary during the anatase-to-rutile transformation (600–800 °C) and decreases quickly to 29 wt% on calcination at 1000 °C.

While it is generally agreed that sol–gel syntheses yield more amorphous material than conventional solid-state synthesis, it was presumed that these quickly crystallize during calcination. Therefore, a substantial non-diffracting component (29 wt%) even after sintering at 1000 °C was unexpected. Moreover, the relatively high reactivity and/or sorption capacity of aperiodic structures raises questions concerning their role during photocatalysis, and the need to control their quantity, and quantify their influence. The determination of amorphous content in nanocrystalline anatase is not without difficulty, as results may be compromised due to microabsorption. Moreover, small anatase particles have been shown to exhibit significant concentrations of titanium vacancies [16,32], with charge balance maintained by introducing H^+ through conversion of O^{2-} to OH^- in the emptied octahedra (Fig. 11). The resulting sum formula can be written as $Ti_{1-x}O_{2-4x}(OH)_{4x}$ and this possibility has been included in these calculations. However, a detailed analysis of our refinements showed a strong correlation between amorphicity and the titanium occupancy. Both the lattice parameters *a* and *c* dilate with increasing crystal size (Fig. 5) in agreement with Grey and Wilson [16] who used a combination of experimental data and density function theory calculations to show that this trend correlates with the concentration of titanium vacancies. Anatase being constructed of distorted, edge sharing TiO_6 octahedra, has the highest degree of polyhedral condensation of all titania polymorphs. The shortest titanium–titanium contact (3.04 Å) propagates in the *c*-direction with the strong repulsion between Ti^{4+} cations compensated for by shortening of the shared edges (O–O = 2.66 Å) and expansion of unshared edges (O–O = 2.79 and 3.04 Å). Introducing metal vacancies reduces titanium–titanium repulsions, leads to a contraction of the octahedra, and reduces the length of the *c*-axis. In the case of sol–gel formed anatase, the concentration of titanium vacancies decreases with thermal treatment while particle sizes and the *c*-lattice parameter increase.

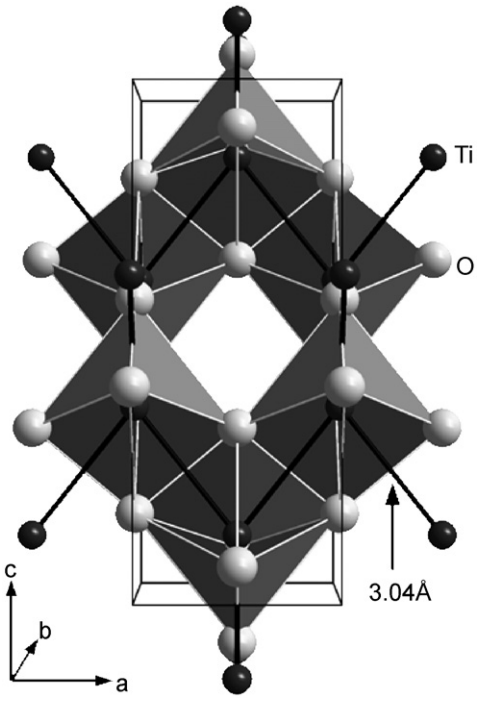

Fig. 11. [010] Projection of the structure of anatase featuring the distorted TiO_6-octahedra and titanium–titanium contacts.

The *c*-axis behaviour in cobaltiferous titania is comparable to the undoped materials [16–17,25], but the *a*-axis trend is subtly different from the data by Li et al. [17] who reported a slight decrease (3.795–3.790 Å) in pure titania while in this study '*a*' is practically constant (3.783 ± 0.002 Å) for all samples, as also observed by Barakat et al. [31] in cobalt-doped material. However, as the changes are small (>0.001 Å) and quickly diminish as the crystallite size increases beyond 10 nm, systematic errors arising from differences in data treatment cannot be discounted. For example, Grey and Wilson [16] used a split Pseudo–Voigt function to model diffraction peak profiles, while this study employed a profile shape based on the fundamental parameter approach. As the empirical function models peak asymmetry without accounting for the shift in peak position, and the fundamental parameters considers both shape and position, the lattice parameters obtained from these methods are slightly different. Neither should differences in the implementation of the Rietveld method in the various programs be discounted.

4.2. Surface chemistry and catalytic activity

The dependence of lattice parameters on metal vacancy concentrations precludes establishing a simple correlation with cobalt incorporation. The substitution of Ti^{4+} (IR = 0.605 Å) by Co^{3+} (0.61 Å) or Co^{2+} (0.745 Å) would lead to dilation, but this effect if present, is masked by increasing cation–cation repulsions as occupancy rises and explicit evidence for replacement of titanium by cobalt in anatase could not be established. However, a combination of surface analysis and catalytic performance is consistent with limited miscibility of cobalt in anatase under the current synthesis conditions.

It has been reported that Ti^{3+} defects, generated by annealing or ion sputtering, may be charge balanced through the creation of oxygen vacancies in a manner that enhances photocatalytic activity [33]. It remains unclear if Ti^{3+} is formed on titania surfaces during processing, or is created via photogeneration of electrons (Ti^{3+} species) and

holes (O^- species) during UV radiation [33]. Lee et al. [10] found that the surface concentrations of Ti^{3+} and OH^- in titania thin films controlled hydrophilicity during photocatalysis, and Liu et al. [34] reported that Ti^{3+} plays an important role as an electron trapping center at the liquid–solid interface in silver-loaded titania powder water suspensions. In this case, it is believed that oxygen radicals transfer electrons to Ti^{4+} and generate Ti^{3+}.

In the current work, the Co $2p^{3/2}$ XPS peak at 780.1–781.5 eV may be attributed to mixed $2^+/3^+$ valences. It is suggested that the appearance of Co^{3+} is due to the air exposure of surface Co^{2+} ions precipitated from the titania that had migrated to the surface during thermal treatment. Illumination may result in the following reversible photoexcitation processes that occur on the titania surface in the present of Co^{2+} and Co^{3+} [35]:

(1) Electron–hole pair generation:
$$(Ti^{4+} - O^{2-}) \overset{hv}{\longleftrightarrow} (Ti^{3+} - O^-)$$
(2) Recombination: $Co^{3+} + hv \rightarrow Co^{2+} + h^+_{VB}$
(3) Photoionization: $Co^{2+} + h^+_{VB} \rightarrow Co^{3+}$
(4) Trapping: $Co^{2+} + hv \rightarrow Co^{3+} + e^-_{CB}$

The recombination process of Co^{3+} shown in equation (2) can limit the formation of photogenerated electrons (Ti^{3+} species) and holes (O^-). By displacing Ti^{3+} and scavenging electrons that would otherwise be available for photocatalysis, surface enrichment in Co^{3+} degrades catalytic activity. Consequently, cobaltiferous catalysts were generally less effective notwithstanding the apparent narrowing in band gap energy. This phenomenon is more significant at higher concentrations ($x > 0.01$) where the majority of cobalt is divalent and partitions to $CoTiO_3$, and for these compositions heat treatment above the anatase to rutile transition temperature completely removed activity.

5. Conclusions

The introduction of cobalt raised the anatase to rutile transformation temperature from ~600 to 700 °C as compared to pure titania prepared from the metal alkoxide. This behaviour is in contrast to the observation of Barakat et al. [29] using $TiCl_4$ as a precursor and serves to emphasize the sensitivity of the product to the reagents used [16]. The role of X-ray amorphous phases and titanium vacancies in controlling phase evolution and photocatalytic activity remains to be fully explored. These investigations show that the amount of non-diffracting phases is both larger and more persistent than generally assumed. While there remain questions as to the exact amount and nature of these aperiodic phases, it can be concluded that they are too prominent to be neglected in a discussion of these materials and their properties. Further studies with neutron powder data are in preparation to address these remaining questions. Additionally, the concentration of titanium vacancies in anatase is not negligible and will significantly impact photocatalytic characteristics. The presence of metal vacancies can be monitored by following the shift in the '*c*' lattice parameter as the crystallite size increases.

Because the abundance of surface Ti^{3+} significantly influences photocatalytic activity its oxidation to Ti^{4+} and the increase of Co^{3+} limits the number of active surface sites. Increasing cobalt content and more complete transformation of anatase-to-rutile at higher temperatures degraded photocatalytic oxidation performance for both methylene blue and formic acid protocols. The degradation of both methylene blue and formic acid over pure titania and Co-doped titanias obeyed pseudo first order kinetics. There was no enhancement of visible light catalysis in cobaltiferous titanias because the miscibility of cobalt was limited, fewer active sites were available, and secondary non-catalytic components such as ilmenite detracted from overall performance.

Acknowledgments

This work was supported through ASTAR Grant 032 101 0023 "Photocatalysts—New Materials and Architectures" and the Singapore-Stanford Program. The manuscript greatly benefited from the critical reviews and advice of Dr. Ian Grey and Dr. Ian Madsen CSIRO Division of Minerals.

Appendix A. Supplementary material

Supplementary data associated with this article can be found in the online version at doi:10.1016/j.jssc.2007.08.021.

References

[1] J. Cunningham, G. Al Sayyed, P. Sedlak, J. Caffery, Catal. Today 53 (1999) 145–158.
[2] S. Parra, V. Sarra, S. Malato, P. Peringer, C. Pulgarin, Appl. Catal. B 27 (2000) 153–168.
[3] K. Nafaveni, G. Sicalingam, M.S. Hegde, G. Madras, Appl. Catal. B 48b (2004) 83–93.
[4] A.L. Linsebigler, G.Q. Lu, J.T. Yates, Chem. Rev. 95 (1995) 735–758.
[5] K. Wilke, H.D. Breuer, J. Photochem. Photobiol. A 121 (1999) 49–53.
[6] D. Dvoranová, V. Brezaová, M. Mazúr, M.A. Malati, Appl. Catal. B 37 (2002) 91–105.
[7] V. Brezová, A. Blažková, L. Karpinsky, J. Grošková, B. Havlinová, V. Jorik, M. Čeppan, J. Photochem. Photobiol. A 109 (1997) 177–183.
[8] H.Y. Liu, L. Gao, J. Am. Ceram. Soc. 88 (2005) 1020–1022.
[9] G. Cristallo, E. Roncari, A. Rinaldo, F. Trifro, Appl. Catal. A 209 (2001) 249–256.
[10] Y.C. Lee, Y.P. Hong, H.Y. Lee, H. Kim, Y.J. Jung, K.H. Ko, H.S. Jung, K.S. Hong, J. Colloid Interface Sci. 267 (2003) 127–131.
[11] M.A. Barakat, H. Schaeffer, G. Hayes, S. Ismat Shah, Appl. Catal. B 57 (2005) 23–30.
[12] M. Iwasaki, M. Hara, H. Kawada, H. Tada, S. Ito, J. Colloid Interface Sci. 224 (2000) 202–204.
[13] J.M. Suvilian, C.S. Erwin, Phys. Rev. B 67 (2003) 144415.

[14] H. Weng, X. Yang, J. Dong, H. Mizuseki, M. Kawasaki, Y. Kawazoe, Phys. Rev. B 69 (2004) 125219.
[15] E. Sancez, T. Lopez, R. Gomz, B. Bokhimo, A. Morales, O. Novaro, J. Solid State Chem. 122 (1996) 309–314.
[16] I.E.N. Grey, C. Wilson, J. Solid State. Chem. 180 (2007) 707–715.
[17] Y. Li, S.H. Lim, T.J. White, R. Withers, H.L. Bing, Mater. Trans. 44 (2003) 1328–1332.
[18] R.W. Cheary, A.A. Coelho, J. Appl. Crystallogr. 25 (1992) 109–121.
[19] TOPAS, User's Manual, Bruker Advanced X-ray Solutions, Bruker AXS, Karlsruhe, Germany.
[20] P. Suortti, J. Appl. Crystallogr. 5 (1972) 325–331.
[21] T.D. Cromer, K. Herrington, J. Am. Chem. Soc. 55 (1955) 4708–4709.
[22] J.K. Burdett, T. Hughbanks, G.J. Miller, J.W. Richardson Jr., J.V. Smith, J. Am. Chem. Soc. 109 (1987) 3639–3646.
[23] K. Kidoh, K. Tanaka, F. Marumo, H. Takei Acta Crystallogr. B 40 (1984) 92–96.
[24] SRM1976 & SRM676, Certificate, National Institute of Standards and Technology, 20 September 2005.
[25] D.M. Többens, N. Stüsser, K. Knorr, H.M. Mayer, G. Lampert, Mater. Sci. Forum 378 (2001) 288–293.
[26] N. Fairley, A. Carrick, The Casa Cookbook, Part 1: Recipes for XPS Data Processing, Acolyte Science, Kinderton Close, High Legh, Knutsford, Cheshire, WA16 6LZ, UK, 2005 pp. 81–222.
[27] Y. Li, S.H. Lim, T.J. White, J. Solid State Chem. 177 (2004) 1372–1381.
[28] R.M. Silversterin, G.C. Bassler, T.C. Morrill, Spectrometric Identification of Organic Compounds, fifth ed., Wiley, Inc., US, 1991, pp. 91–133.
[29] K.S.W. Sing, D.H.R. Everett, A.W. Haul, L.R. Moscou, A. Pierotti, J. Rouquerol, T. Siemieniewska, Pure Appl. Chem. 57 (1985) 603–619.
[30] P.A. Webb, C. Orr, Analytical Methods in Fine Particle Technology, first ed., Micromeritics Instrument Corporation, Norcross, GA, US, 1997, pp. 53–152.
[31] M.A. Barakat, G.S. Hayes, S. Ismat Shah, J. Nanosci. Nanotechnol. 5 (2005) 759–765.
[32] X. Bokhimi, A. Morales, O. Novaro, T. Lopez, E. Sanchez, R. Gomez, J. Mater. Res. 10 (1995) 2788–2796.
[33] T.L. Thompson, J.T. Yates Jr., Chem. Rev. 106 (2006) 4428–4453.
[34] S.X. Liu, Z.P. Qu, X.W. Han, C.L. Sun, Catal. Today 93–95 (2004) 877–884.
[35] R.N. Schwartz, B.A. Wechsler, R.A. McFarlane, Phys. Rev. B 46 (1992) 3263–3272.